Journal of Neural Engineering

PURPOSE-LED PUBLISHING™

Optimal placement of high-channel visual prostheses in human retinotopic visual cortex

To cite this article before publication: Rick van Hoof *et al* 2025 *J. Neural Eng.* in press https://doi.org/10.1088/1741-2552/adaeef

Optimal Placement of High-Channel Visual Prostheses in Human Retinotopic Visual Cortex

Rick van Hoof [1 *] Antonio Lozano [2 *] Feng Wang [2 *]
P. Christiaan Klink [2,3] Pieter R. Roelfsema [2,4,5,6] Rainer Goebel [1,7]

[1] *Department of Cognitive Neuroscience, Maastricht University, Maastricht, the Netherlands*
[2] *Department of Vision and Cognition, Netherlands Institute for Neuroscience, Amsterdam, the Netherlands*
[3] *Experimental Psychology, Helmholtz Institute, Utrecht University, Utrecht, the Netherlands*
[4] *Department of Integrative Neurophysiology, VU University, Amsterdam, the Netherlands*
[5] *Department of Psychiatry, Academic Medical Centre, Amsterdam, the Netherlands*
[6] *Laboratory of Visual Brain Therapy, Sorbonne Université, INSERM, CNRS, Paris, France*
[7] *Maastricht Brain Imaging Centre, Maastricht University, Maastricht, the Netherlands*

* contributed equally

Correspondence to: Antonio Lozano & Rainer Goebel
a.lozano@nin.knaw.nl, r.goebel@maastrichtuniversity.nl

Abstract

Objective: Recent strides in neurotechnology show potential to restore vision in individuals afflicted with blindness due to early visual pathway damage. As neuroprostheses mature and become available to a larger population, manual placement and evaluation of electrode designs becomes costly and impractical. An automatic method to simulate and optimize the implantation process of electrode arrays at large-scale is currently lacking.

Approach: Here, we present a comprehensive method to automatically optimize electrode placement for visual prostheses, with the objective of matching predefined phosphene distributions. Our approach makes use of retinotopic predictions combined with individual anatomy data to minimize discrepancies between simulated and target phosphene patterns. While demonstrated with a 1000-channel 3D electrode array in V1, our simulation pipeline is versatile, potentially accommodating any electrode design and allowing for design evaluation.

Main results: Notably, our results show that individually optimized placements in 362 brain hemispheres outperform average brain solutions, underscoring the significance of anatomical specificity. We further show how virtual implantation of multiple individual brains highlights the challenges of achieving full visual field coverage owing to single electrode constraints, which may be overcome by introducing multiple arrays of electrodes. Including additional surgical considerations, such as intracranial vasculature, in future iterations could refine the optimization process.

Significance: Our open-source software streamlines the refinement of surgical procedures and facilitates simulation studies, offering a realistic exploration of electrode configuration possibilities.

Keywords neurotechnology · visual neuroprosthetics · intracortical electrodes · electrode placement · phosphene mapping · retinotopy · primary visual cortex · population receptive field maps · magnetic resonance imaging · Bayesian optimization · simulation software · large-scale prediction · open-source

1 INTRODUCTION

Advances in neurotechnology are revolutionizing the restoration of lost sensory and motor functions, such as vision, hearing, and movement, through direct brain recording and stimulation (Schalk et al., 2024, Hettick et al., 2022, Sahasrabuddhe et al., 2020, Musk and Neuralink, 2019, Jung et al., 2024, Maynard, Nordhausen, & Normann, 1997).Among these developments, the restoration of a rudimentary form of vision in patients who have become completely blind due to damage in their early visual pathways is particularly relevant (Brindley & Lewin, 1968; Dobelle et al., 1974; Farnum & Pelled, 2020; Nowik et al., 2020; Roelfsema, 2020; Schmidt et al., 1996). The typical approach is to replace a part of the visual pathway with a brain-computer-interface (or visual prosthetic implant) that translates a camera feed into patterned electrical signals that are used to directly stimulate the brain (Normann et al., 2009). Such stimulation of the early visual pathways (retina, optic nerve, thalamus, or visual cortex) elicits dot-like visual sensations with fixed spatial locations known as phosphenes (Brindley & Lewin, 1968; Dobelle et al., 1976; Lee et al. 2000; Maynard 2001; Schmidt et al., 1996). In intact visual systems, the spatial location of a phosphene corresponds to the stimulated neuron's receptive field, the location of the visual field where visual stimuli evoke a response. Receptive fields are predictably organized to represent the visual world in a way that replicates the topography of the retina across several brain areas (i.e., they have a retinotopic organization). This organization is comparable across individuals, but some variability does exist (Benson et al., 2018, 2022). Patterns of phosphenes that together form shapes can be evoked by stimulating several electrodes simultaneously (Chen et al., 2020; Dobelle et al., 1976) or in close temporal proximity (Beauchamp et al., 2020; Bosking et al., 2022; Oswalt et al., 2021). This way, phosphene patterns that are created in real-time, based on a (preprocessed) camera feed, will be able to help blind individuals recover some visual functions that were lost or severely impaired after becoming blind (Fernández et al., 2021, Lozano et al., 2020).

The functional properties of artificial vision with different sets of phosphenes, corresponding to different prosthetic devices, can be studied in seeing volunteers using phosphene simulations. To date, such studies have often assumed high density, uniformly spaced, full field covering phosphene configurations (Avraham et al., 2021; Bollen et al., 2019; S. Chen et al., 2009; Sanchez-Garcia et al., 2020; Steveninck et al., 2020; J. Wang et al., 2021), which is a highly unlikely assumption given the anatomy and functional organization of the human brain. Current state-of-the-art prostheses only cover a small portion of the visual field (Fernández et al., 2021; Niketeghad & Pouratian, 2019), which is often a hardware limitation. With these limitations in mind, it is conceivable that different types of daily activities might require different phosphene configurations. A multi-functional visual prosthesis thus requires a careful selection of electrode designs and cortical location target. For example, a dense foveal coverage would be useful for reading, or recognizing an object in front of you, while peripheral vision may be important for context awareness during navigation (Ghezzi, 2023). Additionally, the number and distribution of stimulation electrodes covering visual space are important determinants. More complex phosphene patterns will require a larger number of electrodes and larger patterns require a broader coverage of visual space. Recent developments in image processing have produced deep learning-based algorithms that allow the most relevant features of a scene to be selectively converted into efficient phosphene patterns (Lozano et al., 2020 , Beyeler & Sanchez-Garcia, 2022, Van Der Grinten, de Ruyter van Steveninck, Lozano et al., 2024). In theory, visual prostheses should allow crucial every-day life activities such as accurate emotion expression recognition (Bollen et al., 2019), navigation (de Ruyter van Steveninck et al., 2022; Lu et al., 2014; Perez-Yus et al., 2017; Vergnieux et al., 2017; L. Wang et al., 2008), object recognition (Li et al., 2018; Lu et al., 2014; Macé et al., 2015; Sanchez-Garcia et al., 2018; Xia et al., 2015) and even motion detection (Chen et al., 2020; Perez-Yus et al., 2017) to be reestablished after vision loss.

Recent advances in biologically plausible simulations of cortical stimulation-evoked phosphenes allow us to realistically study the functional properties of visual cortex-based phosphene vision (Van Der Grinten, de Ruyter van Steveninck, Lozano et al., 2024, Fine, I. and Boynton, G.M. 2024), and to simulate and optimize targeted implant visual coverage, as we demonstrate in this work. An ideal phosphene coverage throughout the visual field would likely require many stimulation sites in a brain structure that encodes the entire visual field. However, it remains unclear how phosphenes evoked by stimulation of different hierarchical areas of the visual cortex perceptually combine (Schiller et al., 2011; Schmidt et al., 1996). A major question for all neuroprosthetic approaches is where to interface with the brain. The broad retinotopic organization of the visual brain puts forward many potential targets for implantation, each with their own challenges (Fernández and Normann, 2016). Contemporary approaches therefore typically target a single functional area. Candidate structures are the retina, lateral geniculate nucleus (LGN) and cortical areas V1 (Fernández and Normann, 2016) to higher order regions like V2, V3, V4 and hMT.

Previously, Beyeler et al. (2019) demonstrated computational models of phosphene vision to optimize surgical placement of retinal implants, estimating that up to ~55% of axonal activation could be avoided, improving the quality of the modeled visual percepts. Bruce and Beyeler (2022) utilized dictionary learning alongside phosphene vision models to enhance expected visual coverage and effective resolution for Argus II users, highlighting the crucial importance of

optimization planning in implant design (Beyeler et al., 2017; Granley and Beyeler, 2021). Another candidate structure, the LGN, represents the entire visual space in a relatively small volume of brain tissue, and phosphene perception in non-human primates has been demonstrated by Pezaris and Reid (2007). However, given its location deep in the brain, an LGN visual prosthesis would require long electrode shanks with a high number of densely placed electrodes at the tip.

The primary visual cortex (V1) lies more superficial, making it an interesting candidate for a visual prosthesis. Electrical microstimulation of an electrode located in V1 produces a phosphene percept which location closely matches the Receptive Field (RF) of the affected neurons (Winawer, J. & Parvizi, J., 2016, Bradley, D. C. et al., Davis, T. S. et al. 2005, Chen et al., 2020). The functional organization of basic visual features such as columnar orientation selectivity and color selectivity is well established in V1 and its position early in the visual processing hierarchy might allow higher level areas in to process more complex visual features, such as motion (Salzman et al., 1990) or faces (Mundel et al., 2003) in a relatively natural way. The feasibility of using large-scale V1 stimulation to generate phosphene-based pattern vision was recently investigated in rhesus monkeys (Chen et al., 2020, 2023) with a 1,024-channel count cortical prosthesis. Human cortex, however, has a lot more gyrification and substantial individual differences in the surface area of visual cortices (Benson et al., 2021). The functional organization of early visual cortex is, however, relatively predictable across individuals as long as the individual anatomy is known (Benson & Winawer, 2018; Rosenke et al., 2021; L. Wang et al., 2015). The ability to derive function from anatomy is especially important in blind patients, as conventional fMRI localizers based on visual input cannot be used. The functional organization of an individual's brain, together with the electrode design and placement, will ultimately determine what kind of phosphene maps a visual prosthesis can generate.

At this moment, visual prosthetic developments are primarily focused on patients with late-onset blindness because 1) these individuals have experienced vision at some point in their lives and are most aware of their sensory loss, and 2) their visual brain is believed to have developed typically, maintaining the necessary connectivity for these approaches to be effective (Heitmann et al., 2023). In addition to solving scientific, engineering and clinical challenges, it is crucial to not only create technically effective devices but to also align neural implant developers' perspectives with the needs and expectations of implantees (Nadolskis et al., 2024, van Stuijvenberg et al., 2024). There is, however, a lack of methodologies to predict, optimize and evaluate the impact of electrode design and placement in visual field coverage in large patient populations efficiently.

Our comprehensive and scalable method to simulate andoptimize the placement of electrodes for a visual prosthesis incorporates 1) the individual anatomy that predicts functional visual maps, 2) flexibility in electrode design, and 3) a preset phosphene map one aims to obtain with the prosthesis. Our pipeline is open-source and automatically finds the electrode configuration that optimally matches a preset 'ideal' phosphene map within these constraints. Because the pipeline uses the individual brain anatomy as a starting point, it can also be used in blind subjects after obtaining an anatomical MRI scan. The optimal location and insertion angles of configurable electrode array models are determined with a Bayesian optimization procedure. This algorithm efficiently minimizes a cost function that considers the electrode yield in grey matter, the visual field coverage of the predicted phosphene map, and the similarity in density distribution between the preset target phosphene map and the predicted phosphene map based on the current implantation parameters. We explore the feasibility of an ideal full-field phosphene coverage, and further demonstrate our pipeline by targeting specific subareas of the visual field within a set of practical surgical constraints. In our examples, model parameters and implant location were jointly optimized for a 3D electrode array containing a thousand contact points equally distributed over a 10x10x10 grid of contact points aimed to be implanted in V1. The general procedure, however, allows for any electrode design and can easily be applied to other or multiple brain areas. We validate our method on 362 human hemispheres using anatomical and retinotopy data from the Human Connectome Project 7T retinotopy dataset (Benson et al., 2018).

2 METHODS

2.1 Preprocessing of the Human Connectome Project 7T retinotopy dataset

Data was obtained from the Human Connectome Project 7T retinotopy dataset (Benson et al., 2018). T1-weighted (T1w) and T2-weighted (T2w) structural scans at 0.7-mm isotropic resolution were processed using the FreeSurfer image analysis suite (version 7.2; http://surfer.nmr.harvard.edu). Subject brains were inflated and aligned to FreeSurfer's anatomical *fsaverage* atlas.

The inferences made in this work are based on the retinotopic data described by Benson & Winawer (2018). In brief, MRI data was acquired using a Siemens 7T Magnetom actively shielded scanner and a 32-channel receiver coil array with a single channel transmit coil (Nova Medical, Wilmington, MA) at a 1.6mm isotropic resolution and 1s TR (multiband acceleration 5, in-plane acceleration 2, 85 slices). The population receptive field (pRF) maps describe the location and the size of the receptive field for each 1mm isotropic voxel (see Benson et al. (2018) for descriptions of pRF models used). pRF surface maps based on empirical data in Freesurfer fsaverage space were warped to individual space using Freesurfer's *mri_surf2surf* function. Bayesian inference of the retinotopic maps was performed using Neuropythy's *register_retinotopy* command (https://github.com/noahbenson/neuropythy). This procedure harmonizes the anatomical inference of the pRFs, the Benson 2014 atlas (Benson et al., 2014) and experimental data (Benson & Winawer, 2018) comprised of retinotopic responses to visual stimuli up to 8 degrees eccentricity. Note that the Benson 2014 atlas predicts maps up to 90 degrees eccentricity, however only the inner 20 degrees of eccentricity in V1, V2, and V3 have been empirically validated.

2.2 Pipeline for optimization of electrode grid placement

Our strategy to optimize electrode placement is to minimize the difference between a 'target' phosphene distribution (TP) and a 'predicted' phosphene map (PP) that we infer from virtual placement of electrodes into a brain model with probabilistic or measured retinotopic maps. This difference was quantified and minimized by calculating the loss with a Bayesian search algorithm (scikit; Pedregosa et al., 2011). An example of the electrode design (and its simplification) used for the simulations is displayed in figure 1A. The main input variables of the optimization function were the angles *alpha* (pitch) and *beta* (yaw), which define the insertion trajectory of the virtually placed implant. This insertion trajectory was determined by finding the intersection between the insertion point on the cortical sheet and the centroid of the calcarine sulcus (CS) at the angles *alpha* and *beta* (Figure 1A-B). The centroid, or geometric center, was calculated using the medians along the three dimensions of the CS volume. Importantly, the CS has been reported to be a reliable estimate of the location and total volume of the human primary visual cortex (Gilissen & Zilles, 1996). To test whether this is also the case in the HCP dataset, the CS volume was determined by Freesurfer's cortical parcellation algorithm (Desikan-Killiany Atlas) and compared to the volume of V1 (all voxels in the cortical ribbon of the V1-parcel determined by the pRF model), see supplementary figure S1. The range of insertion angles were restricted so that the insertion trajectory cannot intersect with the other hemisphere, and it excludes unrealistic surgical approaches (e.g. insertion in an anterior - posterior direction).

For many combinations of angles, a portion of the electrode grid would end up outside of the cortex. In case any electrode was out of bounds, the configuration was flagged as invalid, and a penalty was assigned in the optimization procedure. An extra parameter (*shank offset)* was added to the optimization function to enable the distance between the insertion point on the cortical surface and the first contact point on the electrode shank to vary (Figure 1A). To further vary cortical depth, the final parameter *shank length* was included in the search for optimal electrode coverage, density and yield (Figure 1A). Note that the longer the shanks, the higher the space between contact points, affecting the density of contact points and thus the space between the phosphenes in visual space. We constrained the cortical depth of electrodes to 8 cm, representing approximately half the brain's average length (17 cm) and enabling access to deeper structures, such as regions corresponding to higher eccentricities, from a broad range of insertion angles (Yang et al., 2020). See Table 1 for an overview of the parameters and the respective ranges. Furthermore, the search can be used to optimally place electrodes in a specific region of interest (ROI). Neurons in V1 have a smaller receptive field size compared to higher visual areas (Benson et al., 2021), potentially allowing denser phosphene maps. During Bayesian search, some parameter combinations may position electrodes outside the brain. To ensure valid placements within the cortical volume, we penalized configurations with contact points outside V1. Instead of excluding these cases outright, the penalty magnitude controls the extent to which the algorithm can explore boundary regions, potentially leading to better solutions near anatomical limits. For each set of parameters, or cycle of the optimization pipeline (Figure 2), the electrode-grid is virtually positioned to match the trajectory set by the insertion angles. The predicted

phosphene map is then extracted from the intersection of the electrode coordinates and the voxels of the retinotopic map. Each individual electrode that is located in a retinotopically defined map yields a phosphene on a 500-by-1000-pixel image-grid, ranging up to 90 degrees visual angle. Note that the resolution of the image-grid onto which we project the phosphenes impacts the simulation speed. However, if the resolution is too low, the accuracy of the loss function is compromised. To simplify the simulation, we fix the spread of stimulation current to the voxel size of the retinotopic map ($1mm^3$). Phosphenes are modeled as 2-D Gaussian spots of light with standard deviation ranging from 0.2 up to 3 visual degrees, depending on the cortical magnification factor and a simulated stimulation amplitude of 100 micro-amps (Tehovnik et al., 2005; Wang et al., 2008). Finally, the process is repeated for a new set of parameters up to 100 times (separately for each hemisphere). The entire procedure is illustrated by the images in figure 1 and the flowchart diagram in figure 2.

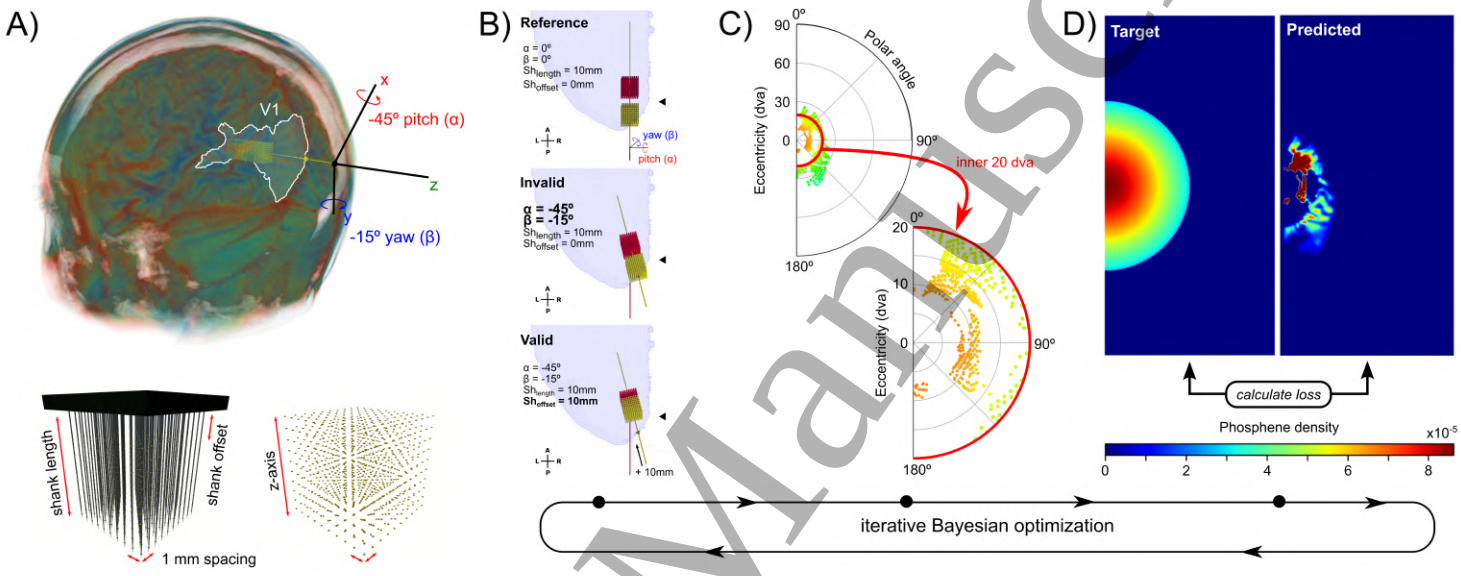

Figure 1. Overview of electrode optimization pipeline. The Bayesian search algorithm determines the next set of parameters based on a loss function with several components (see Methods), and the process is repeated until the optimal set of parameters is found for a specific target phosphene configuration. A) illustration of electrode placement (top) and electrode-grid configuration parameters (bottom). B) The red grid only serves as a reference and is centered on the center of the left calcarine sulcus (black triangles). The implant position (yellow grid) is calculated based on alpha (pitch) and beta (yaw) relative to the reference grid. For a new set of parameters, the resulting configuration can be either valid (left) or invalid (center) when contact points are located outside of the brain. In the 'valid' example, the contact point closest to the base is located 10mm from the point where the shank penetrates the cortex. The base is located on the surface of the brain and serves as the anchor point for the shanks. C) Each contact point potentially evokes a phosphene in the polar angle plot. The individual phosphenes are modeled as 2-D Gaussians on a 500-by-1000-pixel phosphene map. Color codes for eccentricity. D) One of the loss terms is the Hellinger distance between the probability distributions of the simulated phosphene map (left) and the target phosphene map (right).

2.3 Bayesian optimization

Bayesian optimization has become an attractive method to optimize expensive to evaluate black box functions which are derivative-free and possibly noisy (Shahriari et al., 2016). Bayesian methods have been proven useful in several neurotechnology applications such as neurostimulation interventions (Choinière et al., 2024, Losanno et al., 2021, Bonizzato et al., 2023) and human-in-the-loop optimization of visual encoding in retinal prosthesis (Granley et al., 2023). The algorithm iteratively evaluates a probabilistic model for which a cheap probability function f based on the posterior distribution is optimized before sampling the next point. The function objective is considered as a random function (a stochastic process) on which a prior is placed. Here, the prior is defined by a Gaussian process capturing our beliefs about the function behavior. Function evaluations are treated as data and used to update the prior to form the posterior distribution over the objective function. The convergence of the optimization algorithm was accelerated by setting an initial sampling point for which it was known that the resulting grid would hit some portion of V1. We chose to position the center of the electrode grid at the centroid of the calcarine sulcus with initial parameters 0° *alpha*, 0° *beta,* 20mm *shank length* and 25mm *shank offset*. The model can also be run without such prior knowledge of the objective function, but it will likely take more iterations to converge.

Table 1: Parameters optimized by the Bayesian optimizer. Beta values correspond to the left hemisphere. For the right hemisphere, the range is $[-110°, 15°]$.

Parameter	Range	Unit
Alpha	$[-90°, 90°]$	degrees
Beta	$[-15°, 110°]$	degrees
Offset from base	$[0, 40]$	mm
Shank length	$[10, 40]$	mm

2.4 Loss function

The loss function comprised three linearly weighted terms that together indicate the difference between a desired phosphene map and the phosphene map predicted from sampling the pRF parameters at the location of the 1000 simulated electrodes in the brain. Below, we explain each loss term and its meaning in the context of the optimization goals. We chose to emphasize the contribution of visual field coverage and phosphene distribution relative to the absolute number of electrodes in V1. However, weights *a*, *b* and *c* can be tweaked depending on the desired outcome. A fourth loss term is added to demonstrate an additional safety constraint in case intravascular data is available (see section 2.4.4: Vessel avoidance.

$$Loss = aDC + bY + cH + dV \quad (1)$$

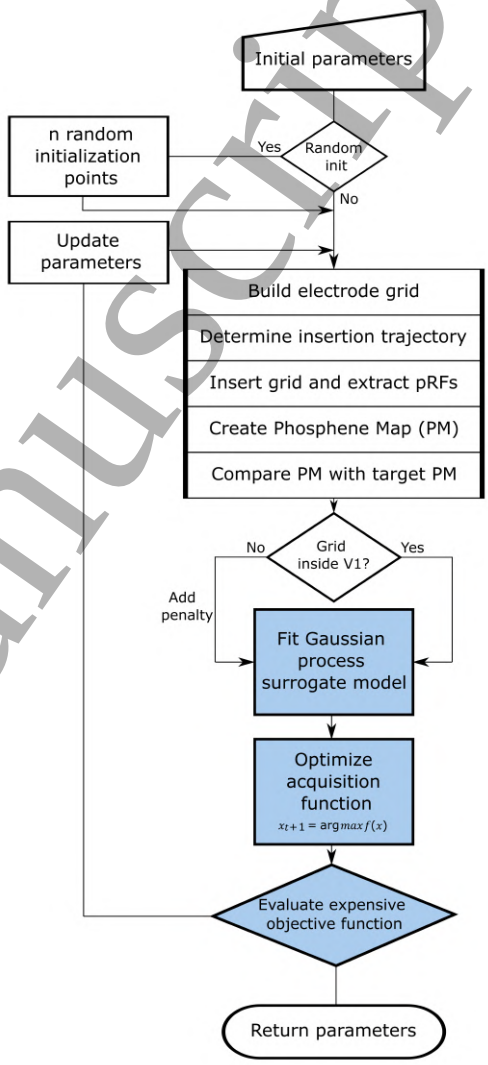

Figure 2. Bayesian Optimization Pipeline for Virtual Electrode Placement.

The optimization process begins with parameter initialization, followed by building an electrode grid, generating a phosphene map (PM) based on the insertion trajectory's endpoint, and comparing it with the target PM. If the grid extends beyond the target area (V1), a penalty is applied. The process then iterates using a Gaussian process surrogate model, where the next iteration point, x_{t+1}, is selected by maximizing the acquisition function $f(x)$. This iterative process continues until convergence. Rectangles denote processes, while diamonds represent decision points.

2.4.1 Sørensen–Dice coefficient

The dice coefficient (*DC*) is a measure of overlap between two datasets. DC was computed on the binarized target phosphene map (TP) and a binarized version of the predicted phosphene map (PP). Each pixel was set to 1 if they contain phosphene activation and 0 if they do not. |TP| and |PP| represent the number of elements in each set. The Sørensen index equals twice the number of elements common to both sets divided by the sum of the number of elements in each set. Dice is included to obtain phosphene maps that are localized in the desired visual region.

$$DC = \frac{2|TP \cap PP|}{|TP| + |PP|} \tag{2}$$

The DC term measures the extent of visual field coverage, regardless of the intensity or distribution of the phosphenes. Binarization simplifies the metric to focus solely on whether specific regions of the visual field are activated, thereby facilitating the evaluation of coverage completeness. Additionally, it enhances robustness to noise and intensity variations, preventing minor differences from disproportionately influencing the results. This approach aligns with the practical goals of prosthesis design by ensuring critical regions of the visual field are covered to support essential tasks, such as navigation and object recognition, in cases where coverage is more important than phosphene-level intensity differences.

2.4.2 Yield

Yield indicates the proportion of electrodes that can evoke a phosphene. We aim this to be as high as possible, thus allowing the implant to achieve high spatial resolution. Contact points outside of the targeted region are penalized by adding a constant to this loss term.

$$Y = \frac{n_{hits}}{n_{contactpoints}} \tag{3}$$

2.4.3 Hellinger distance

The Hellinger distance (*H*) quantifies similarity between two probability distributions and is defined as the square root of the expected squared difference between the square roots of the probability distributions.

$$H(P,Q) = \sqrt{\sum \left(\sqrt{P} - \sqrt{Q}\right)^2} \tag{4}$$

Hellinger distance is especially suitable for comparing normalized discrete probability distributions in machine learning as it is restricted to the range between 0 and 1. *P* refers to the probability distribution of the target phosphenes, and Q to the distribution of predicted phosphenes. The maximum distance 1 is achieved when *P* assigns probability 0 to every set to which *Q* assigns a positive probability, and vice versa. *H* will reward parameter sets for which the virtually implanted electrodes yield a phosphene map with the desired density distributions and penalize density distributions that diverge from the target map.

While the Sørensen–Dice coefficient assesses coverage, the Hellinger distance metric complements it by simultaneously considering the distribution and intensity of phosphenes across the visual field. This division of roles ensures that each term addresses a distinct aspect of the optimization, with the binarized dice coefficient measuring "where" activation occurs and the Hellinger distance evaluating "how" it is distributed. Together, dice coefficient, yield and Hellinger distance provide a balanced approach to optimizing both the quantity (coverage) and quality (distribution) of phosphene placement.

2.4.4 Vessel avoidance

The Vessel avoidance (V) term can be incorporated into the loss function when intravascular data is available. This term penalizes electrodes positioned near blood vessels by utilizing two components: *confidence-weighted distance* and

a *hard constraint* defined by a minimum vascular distance threshold. V combines exponentially decaying penalties based on the proximity of each electrode to nearby vessels and a strict penalty for electrodes within the safety threshold, measured in millimeters. The term is expressed as follows:

$$V = \frac{1}{N} \sum_{i=1}^{N} \left(\sum_{j=1}^{k} \left(e^{-\frac{d_{ij}}{\lambda}} \cdot \alpha + c_j \cdot \beta \right) \right) + s \cdot \mathrm{I} \tag{5}$$

where:

- V: Vessel avoidance term.
- N: Total number of electrodes.
- k: Number of nearby vessel voxels considered (neighbors).
- d_{ij}: Euclidean distance from electrode i to vessel voxel j.
- λ: Decay constant controlling how strongly closer vessels are penalized.
- c_j: Confidence of vessel presence at voxel j (ranging from 0 to 1).
- α: Weighting factor for the distance decay term (`decay_factor`).
- β: Weighting factor for the confidence term (`confidence_factor`).
- s: Minimum vascular safety threshold (in mm).
- I: Number of infractions (count of vessel voxels within the safety threshold).

By default, this term is not included in our automatic optimizations due to the absence of intravascular data in the HCP dataset. However, its functionality is demonstrated in Section 3.4, where it is applied in the fsaverage brain using a mid-to-large brain vessel atlas (Viviani, 2016).

2.5 Phosphene maps

There is a (hardware-based) limit to the extent of visual field coverage within the parameters of the single electrode array we use here (evident from Figure 3 and 4). The exclusive consideration of 'full coverage' does not provide sufficient insight into the procedure's accuracy in targeting specific subregions of the visual field. In addition, different cognitive functions may differentially rely on different subregions of the visual field and individual patients may choose a visual field coverage that matches their preferences. Therefore, we demonstrated the spatial specificity of our pipeline by targeting four distinct target coverages where the density of the map increases progressively moving from the periphery towards the center (see Figures 1D, 5 and 6 for visual references):

1. *full target*: covers 0-90° eccentricity.
2. *inner target*: covers 0-45° eccentricity.
3. *upper target*: covers 0-90° eccentricity and 0-45° polar angle.
4. *lower target*: covers 0-90° eccentricity and 135-180 ° polar angle

Simulated phosphenes were inspired by recently published phosphene simulation work (Van Der Grinten, de Ruyter van Steveninck, Lozano et al., 2024) which integrates electrophysiological, modeling and psychophysics knowledge across non-human primates and clinical work. Our simulated phosphenes were scaled by eccentricity using flattened cortical maps to determine the Cortical Magnification Factor (CMF), as described by Schwartz (1983), and the multi-area visuotopic map complexes in the macaque striate and extrastriate cortex identified by Polimeni et al. (2006). Default mapping parameters were taken from Horton and Hoyt's revision of the classic Holmes map (1991), but patient-specific maps or approximations of Benson et al.'s findings (Benson et al., 2018) could be used. The cortical magnification factor (CMF) for each electrode location was computed to determine the degrees of visual angle covered per mm of tissue surrounding each electrode. Using a simulated stimulation amplitude of 100 micro-amps, the amount of tissue activated was estimated based on the function and parameters established by Tehovnik and Slocum (2007).

$$M(e) = k\left(\frac{1}{e+a} - \frac{1}{e+b}\right)$$

Where:

- M: Cortical Magnification Factor (CMF).
- e: Eccentricity in degrees.
- a, b: Parameters for the visuotopic map ($a = 0.75, b = 120$).
- $k = 17.3$: Scaling factor.

CMF was then multiplied by the activated area to obtain the phosphene size in degrees of visual angle (S).

$$S = M(e) \cdot R_c$$

We then drew a Gaussian distribution onto a phosphene center so that 95% of the Gaussian's activation falls within the phosphene area, with the phosphene diameter equating to 2 standard deviations of the Gaussian.

$$\sigma = \frac{S}{2}$$

$$G(x, y) = \exp\left(-\frac{(x - x_0)^2 + (y - y_0)^2}{2\sigma^2}\right)$$

Where:

- G: Resulting Gaussian blob.
- (x_0, y_0): Center coordinates of the phosphene.
- σ: Standard deviation, representing half the phosphene diameter.

2.6 pRF polar density estimation

Probability density functions (PDFs) of group average phosphene maps were defined by computing a non-parametric kernel-density estimation (KDE) using SciPy 1.0 (Virtanen et al., 2020). The group average phosphene maps were created by summing simulated phosphenes of the optimized electrode locations in all subjects. Phosphene maps were created separately for each region of interest (V1, V2, V3, and an all-encompassing 'grey matter' ROI). The polar plots in figure 6 show the average density estimate across subjects for different visual field targets. Density was scaled by the maximum to allow for a fair comparison between regions of interest.

2.7 Group average electrode configuration

In addition to the individual approach, i.e. determine the best electrode configuration for each person individually, we also optimized electrode placement based on the average brain. Here, we applied the electrode optimization pipeline to the *fsaverage* brain and the group average retinotopy (averaged fMRI timecourse). Phosphene maps were then predicted for individuals either based on the 'average' or 'individual' parameter estimates. Results were compared to establish the potential benefits of an individual optimization approach (see figure 7).

2.8 Statistical analysis

Repeated Measures Individual Analysis of Variance (RMANOVA) and pairwise post-hoc Tukey's multiple comparison tests were performed using Python library statsmodels v0.14.0 (Seabold & Perktold, 2010). The reported statistical results were Bonferroni corrected by dividing the significance levels by two (the number of individual ANOVA analyses) to correct for multiple comparisons.

3 RESULTS

Optimal electrode placement in primary visual cortex was determined for both hemispheres of 181 subjects from the HCP 7T dataset by minimizing the difference between a desired phosphene map and predicted phosphenes from virtual electrode placements. The feasibility of obtaining maximal visual field coverage is illustrated using data from example subjects (figure 3 and 4). The average results over all individuals are then described using pRF/phosphene density distributions (figure 5 and 6) indicating the probability that a phosphene was evoked in a specific spatial location with the optimized placements parameters. Finally, we compared individualized optimization based on an individual's own brain scan with the general optimization solution based on the group (fs)average brain (figure 7).

3.1 Standardized starting point for the Bayesian search space

In our sample of 181 individuals, we found that the volume of the calcarine sulcus (CS) correlated well with the volume of V1 in both hemispheres (Pearson correlation left hemisphere: $r = 0.95$, $p < 0.001$; right hemisphere $r = 0.87$, $p < 0.001$; figure S1). We used the centroid of the CS as a standardized anatomy based starting point for optimization (with alpha and beta insertion angles set to zero).

3.2 Phosphene maps from optimized electrode placements

We optimized electrode placements for a target phosphene density map with a coverage of 90 degrees and with a density that follows a Gaussian function, corresponding to the entire visual field. Figure 3 provides an example of the best possible placement for our electrode array design, using the trajectory constraints defined in 'Pipeline for optimization of electrode placement', the brain's anatomical dimensions, as well as the predicted phosphene density map. The optimal phosphene map reveals a densely populated area between the first 5 to 20 visual degrees, followed by a coherent spaced-out distribution at higher eccentricities. High eccentricities are notably absent, due to constraints of the electrode array and cortical layout.

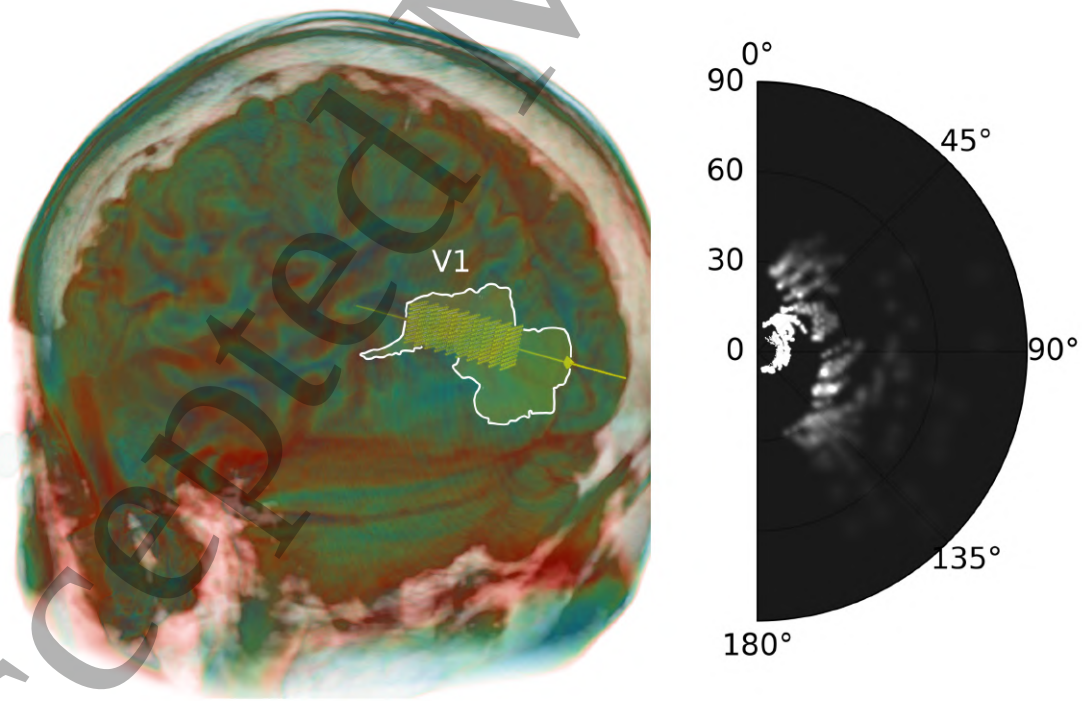

Figure 3. Phosphene configuration in an example subject. The image on the left shows the electrode locations after implantation, based on parameters $\alpha = 13$, $\beta = -15$, shank offset = 13 mm, and shank length = 24 mm. The V1 region of interest (ROI) is indicated by the white delineation. The yellow diamond marks the brain surface where the grid base is positioned. For clarity, the grid base, as well as the shanks/cables connecting the grid base to the electrodes, are not shown. The image on the right displays the simulated phosphene map corresponding to these electrode locations, with intensity reflecting the number of overlapping phosphenes.

Figure 4 shows optimized phosphene locations in two subjects for the full visual field and the inner half of the visual field, along with the best configuration for the *fsaverage* brain. Repeated measures ANOVA revealed a significant interaction on *loss* between *target* and *hemisphere* ($F(3, 540) = 7.1$, $p < 0.001$). We also found a pronounced difference between *left* and *right* hemispheres for *full* target ($M = -0.05$, $p < 0.001$), *lower* target ($M = -0.10$, $p < 0.001$) and *upper* target ($M = -0.07$, $p < 0.001$). Loss was lower for the right hemisphere for all targets, except the inner target (see Figure 4C).

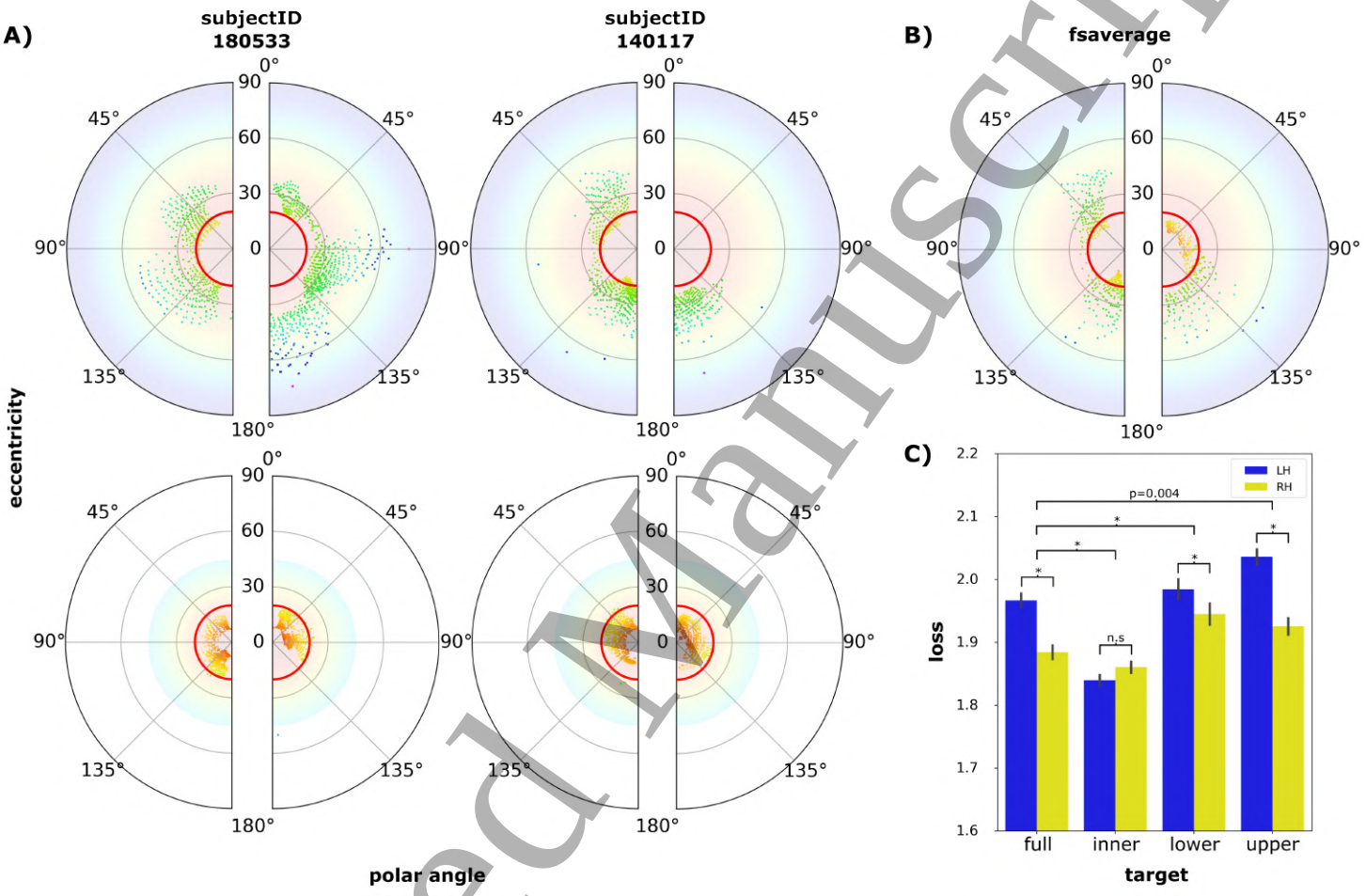

Figure 4. Comparison of individually optimized electrode configurations for the full visual field and foveal target. A) The top row shows phosphene locations in two randomly selected subjects when targeting eccentricities up to 90 degrees (top row) and 45 degrees (bottom row). B) The polar plots (top) display optimization results for the averaged pRF across all subjects in the fsaverage brain. The red lines indicate the first 20 degrees of eccentricity. C) The bar chart (bottom right) illustrates the loss in all subjects across both hemispheres for each target. Error bars represent the standard error [* = $p < 0.001$]. The legend denotes LH = left hemisphere and RH = right hemisphere.

Optimization variability across the population was further evaluated with group-average pRF density functions of predicted phosphenes across the visual field. In figure 5 and 6, pRF density plots are shown per target phosphene map across the regions of interest. We observed a fairly symmetrical phosphene peak distribution across hemispheres, with most phosphenes located quite central in the visual field. Phosphenes obtained for the upper and lower target maps were mostly located in the expected visual quadrants, however a relatively large proportion of these phosphenes came from electrode contacts in V2 and V3. This indicates that even when the algorithm tends to place the grid in V1 for these target regions, frequently no solution could be found where all 1000 electrodes are placed in V1.

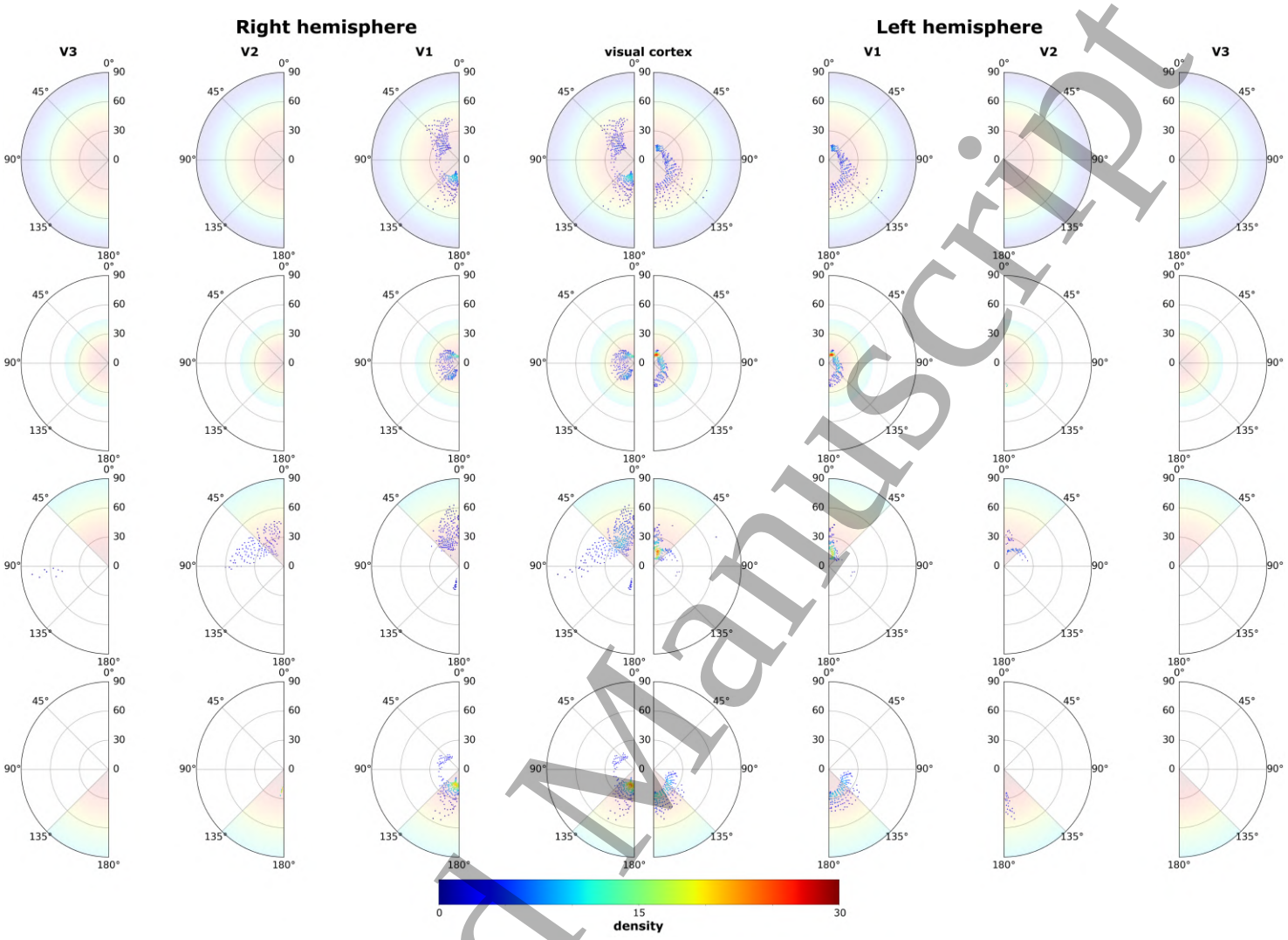

Figure 5. pRF density polar plots in the fsaverage brain. Results after running the pipeline on subject average population receptive field (pRF) maps projected on the fsaverage brain. The color indicates the density (as determined by Gaussian kernel density estimation) of simulated phosphenes in visual space. For reference, the target phosphene map is shown on the background of each plot. For the lower and upper target, even the best solution places a notable amount of electrodes in V2.

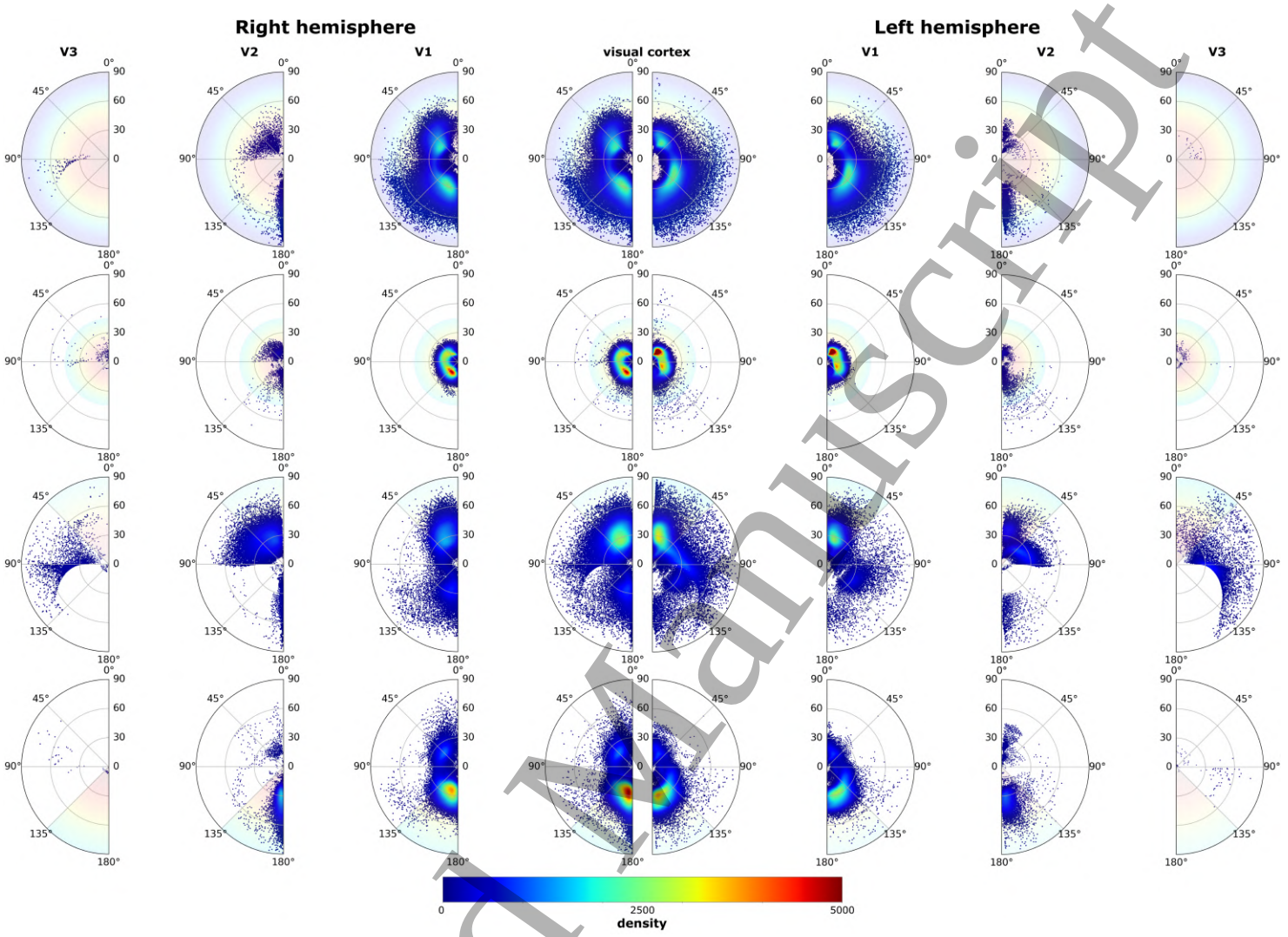

Figure 6. Group average pRF density polar plots. The center plots present a summary of all population receptive field (pRF) locations in either the left or right hemisphere after optimizing electrode configurations across all subjects. The color represents the density, determined using Gaussian kernel density estimation (KDE), of simulated phosphenes in visual space. For reference, the target phosphene map is displayed in the background of each plot. Depending on the target visual field region and individual variations, many electrodes are placed in V2 and V3.

3.3 Group average optimization versus individual optimization

For a less computationally expensive, and thus faster way to design an electrode grid, it is possible to optimize the placement of electrodes on the average brain and then virtually implant this configuration in all individuals. In figure 7 this group average approach is compared with the results from the individualized optimization approach. Each element of the loss function is shown separately for a more detailed description of differences in visual coverage. Post hoc comparisons using the Tukey HSD test indicated that the individually optimized approach significantly outperformed the average approach for phosphene yield ($M = 0.03$, $p < 0.001$), phosphene map coverage ($M = 0.18$, $p < 0.001$), as well as Hellinger distance ($M = 0.08$, $p < 0.001$). See supplementary materials (figure S3) for single-subject examples.

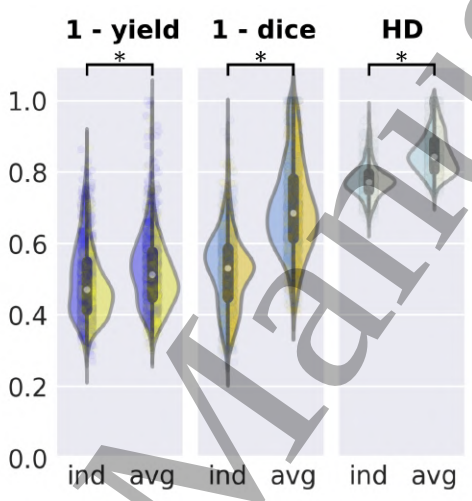

Figure 7. Superior visual coverage for individually fine-tuned electrode placement. The violin plots illustrate the three loss terms, with each half representing results for the left (blue) or right (yellow) hemisphere. Configurations based on individually optimized parameters (ind) result in significantly more electrodes successfully placed in V1, greater phosphene coverage, and a more accurate density distribution compared to an average electrode configuration (avg). HD represents the Hellinger Distance. [* = p<0.001].

3.4 Intravascular-aware optimization

When intravascular data is available e.g. by obtaining a 3D Time-of-Flight Magnetic Resonance Angiography sequence (Sehgal & Farooq, 2021) for each blind individual, a vascular avoidance term can be added to the optimization (see Methods 2.4.4 vessel avoidance). This loss term accounts for blood vessels by adding a penalty to each contact point depending on how close they are to segmented blood vessel voxels, thus pushing the Bayesian optimization towards safer solutions. In addition, when the array is closer to a blood vessel voxel by lower than a threshold set by the user e.g. 2mm, 5mm, 10mm, the solution is rendered invalid. To demonstrate the use of this safety term, we simulated an implantation within the fsaverage brain, incorporating mid-to-large blood vessel reconstructions based on the atlas by Viviani (2016) aligned to the fsaverage brain. Figure 8 shows how the safety term penalizes risky locations.

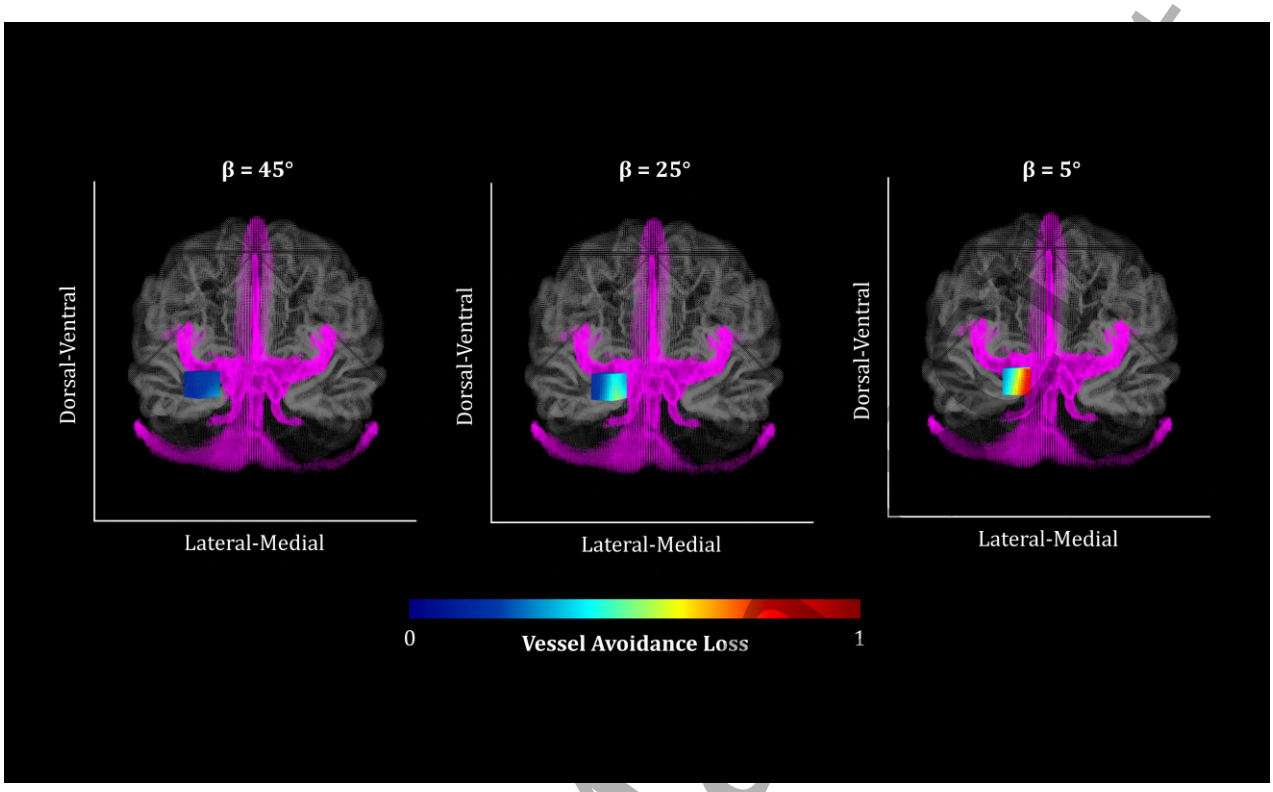

Figure 8. Intravascular-aware optimization. Intravascular data from Viviani (2016) was aligned to the fsaverage brain, with the loss function term calculated for each individual voxel in V1. The images, arranged from left to right, illustrate increasing beta angles. As the array is shifted closer to the superior sagittal sinus, the vessel avoidance loss correspondingly increases.

4 DISCUSSION

Restoring a rudimentary form of vision in blind patients is an ambitious aim for neuroscience and neural engineering that has recently gained a lot of attention. Visual prostheses that interface directly with the brain may one day be a realistic treatment option for blindness that results from damage to the early visual pathways Normann et al., 2009; Fernández et al., 2021; Roelfsema, 2020; Rosenfeld et al., 2020). However, the development of such a treatment comes with significant challenges. The method of optimizing electrode placement that we present here addresses several of these, allowing to optimize the design and placement of electrode arrays to obtain a functional implant with coverage and resolution that matches a pre-defined target, within predetermined boundaries for surgical implantation.

Pioneering research by Chen et al. (2020) demonstrated that high-channel count, dense visual coverage is achievable in non-human primates using multiple Utah arrays, with up to 9 degrees of coverage in V1 and up to 15 degrees in V4. Preliminary findings with the Intracortical Visual Prosthesis (ICVP); Dagnelie et al., 2023,Barry et al., 2023), show the stable use and phosphene mapping of up to 25 wireless floating microelectrode arrays (WFMAs), each with 16 stimulating electrodes (up to 400 electrodes distributed around the available surgical area). While distributing electrodes over multiple (smaller) electrode arrays shows high potential of improving visual coverage, challenges emerge when trying to optimize the placement of multiple interdependent arrays. For example, they cannot physically occupy the same space, and their implantation trajectories need to be compatible, which is especially relevant for deeper electrodes. In the case of non-wireless implants, extra space for cables (and occasional encapsulation and gliosis) should be taken into account (Chen, 2023).

Our current approach can be expanded to place multiple electrode arrays in a serial manner, however more elaborate optimization procedures may be needed. In sighted human volunteers, and using surface electrodes located on the medial wall of the occipital lobe near the calcarine sulcus Beauchamp et al., (2020) reported relatively high eccentricities with a mean reported phosphene location of (azimuth 13.3°, elevation 2.1°). In the human brain, achieving higher visual visual field coverage ($> 30°$) in V1 will likely involve long penetrating shanks deep into the sulcus, according to pRF estimations (Benson et al., 2018). Even with hypothetical high-channel count, long-shank arrays such as those used in our simulations, covering the entire visual field with high spatial resolution remains a significant challenge. To achieve high visual coverage while minimizing both acute surgical tissue damage and chronic encapsulation, ultra-thin, ultra-flexible electrode arrays have emerged as a promising alternative to rigid electrodes. These arrays have demonstrated impressive results in neural recording and chronic tracking of neural activity (Musk, 2019). Notable advancements include flexible depth electrodes capable of recording from up to 128 channels at depths of up to 10 cm in human brain tissue (Zhao et al., 2024). Furthermore, ultra-flexible arrays have been shown to generate low-threshold detectable visual percepts in mice (Lycke et al., 2023; Orlemann et al., 2024) and achieve high-quality neural recordings in the visual cortex of non-human primates (Merken et al., 2022). These developments highlight the potential of ultra-flexible electrodes to enhance visual coverage and improve the longevity and safety of cortical visual prostheses. Alternatively to penetrating flexible electrodes, a fully-wireless, $50\,\mu\mathrm{m}$-thick flexible μECoG chip with 65,536 recording and 16,384 stimulation channels has been demonstrated to provide stable chronic recordings (including cortical visual responses), and stimulation capabilities in porcine and non-human primates by Jung, T. (2024).

Our data-driven approach optimizes electrode placement using simulated phosphenes based on individual anatomy, minimizing the difference between the simulated phosphene patterns and a predefined target layout. In this work, we chose to demonstrate our optimization pipeline using the center of the Calcarine Sulcus as the insertion target, and established a series of design parameters (shank lenght and shank offset) and implant positioning parameters (alpha and beta angles) as a search space. However, implant designers and researchers can easily select their own insertion targets, design parameters, and perform any geometrical transformation and positioning of their implant, as long as the implantation method is surgically feasible.

Even though we set the algorithm to optimize electrode placement in V1, a fraction of the contact points ended up in V2 and V3. The algorithm also has the capacity of optimizing placement based on multiple visual areas, while it is currently unknown how phosphenes that are evoked in distinct visual areas are perceptually combined into patterns. Future studies should address this question, as it would greatly expand the possible configurations for a cortical visual prosthesis. About half of the electrodes in our simulations were located inside grey matter, with most of the remaining electrodes likely located in white matter. Here, we assumed that white matter stimulation cannot effectively create useful phosphene percepts. This assumption is partly based on the lack of a clear prediction for the retinotopic organization of white matter. However, since these fiber paths do connect visual areas and carry visual information, further research might help to understand the perceptual effects of white matter stimulation.

The predicted phosphene maps were generally closer to the target distribution for the right hemisphere for

all targets, except the inner target. This difference might be related to anatomical hemispheric differences (see also supplementary figure S1). Our results also demonstrated that while it is possible to base electrode placement on the optimization solution in the average brain, an individually optimized approach performed significantly better. This finding underscores the importance of tailoring electrode placement and design to the specific anatomical characteristics of each individual (Beyeler et. al, 2019, Bruce and Beyeler, 2022). By considering individual variations, we can achieve better outcomes and optimize visual restoration for each patient.

The loss terms implemented in our approach were chosen for interpretability and ease of use. However, they can easily be customized, replaced, or expanded to match the needs of the designers and users. With the example electrode array used here, array placement results were more successful for the foveal (inner) target region, compared to the more peripheral (full, upper and lower) target regions. This is a direct consequence of the higher eccentricities being located deeper along the calcarine and requiring longer shanks to reach them, which automatically increases the electrode spacing along the shank. In addition, a relatively large part of cortex is dedicated to central vision (low eccentricities) compared to peripheral vision (known as cortical magnification). A more suitable approach to get coverage from the peripheral visual field is to target different sections of the visual field with multiple electrode arrays and/or in different visual areas. Retinotopic maps are ubiquitous along the visual cortical hierarchy (Wandell et al., 2007), but receptive field sizes increase towards higher areas, reducing the spatial resolution of potential phosphene vision. Importantly, and to reiterate a previous point, it is currently unknown how simultaneous stimulation across hierarchically different visual areas perceptually combines.

The accuracy of the phosphene map predictions in our pipeline crucially depends on 1) the precision and the spatial resolution of the underlying population receptive field maps/atlas. There is an accumulative uncertainty that stems from alignment and extrapolating data from seeing individuals to blind individuals. 2) the assumptions of the phosphene simulation algorithm. A possible improvement to the first matter could be to acquire higher quality pRF data. The availability of higher field strengths could potentially yield scans with higher resolution. It is highly recommended to obtain detailed individual anatomy using a high-resolution MRI scan whenever possible. Retinotopy can then be estimated based on individual anatomy and group-average (probabilistic) pRF maps. Additionally, simulations can be improved by incorporating blood vessel mapping through techniques such as 3D Time-of-Flight MR Angiography (Sehgal & Farooq, 2021) and applying the vessel avoidance term demonstrated here to optimize electrode placement.

Recent work in phosphene simulation have pushed forward the biological plausibility and accuracy of these "virtual patients" (van der Grinten, de Ruyter van Steveninck, Lozano, et al. (2024), Fine, I., Boynton, G.M. (2024)). By incorporating decades of research and clinical knowledge on the electrophysiology and psychophysics of phosphene perception, essential elements of phosphene percepts such as the relationship between electrode location, stimulation parameters, temporal history of stimulation and phosphene size, brightness and temporal dynamics can be better predicted. However, there is a long road ahead until the mechanisms of phosphene vision are fully elucidated, and complex shapes, non-linear multi-electrode interactions, temporal interference, feature-specific percetps, multi-area percepts integration as well as inter-individual variability and the effect of neuroplasticity, to name a few, remains a challenge. Future work addressing these and other issues will allow for better planning which will have in account not only the phosphene locations in V1 but more complex perceptual properties that can be elicited with multi-area stimulation, as well as optimize for elements such as cortical inter-electrode distances to account for nonlinear microstimulation interactions.

Moreover, the "optimal phosphene map" achievable with an implant may be different depending on the task to be evaluated, as well as the user's needs and expectations. In order to learn about task-oriented optimal phosphene maps, future virtual implant optimizations could benefit from end-to-end computer vision and simulation pipelines, where the effectiveness of phosphene map configurations in daily life activities can be pre-evaluated using deep neural networks (van der Grinten, de Ruyter van Steveninck, Lozano, et al. (2024), Beyeler, (2022), Küçükoğlu et al. (2022). Moreover, VR settings incorporating the effects of gaze-contingent phosphene simulations (de Ruyter van Steveninck, 2024) can allow for psychophysics and task-driven performance evaluations with sighted subjects. VR phosphene testing allows to evaluate and compare the performance of different electrode locations beyond quantitative metrics such as coverage, and extend its relevance to realistic and diverse scenarios (Beyeler & Sanchez-Garcia, (2022), de Ruyter van Steveninck et al., (2023)) and user needs (Nadolskis et al., 2024, van Stuijvenberg et al., 2024).

Finally, to ensure the robustness and clinical relevance of these simulations, validation should be conducted on a cohort of blind individuals. By acquiring detailed anatomical information, including vasculature, we can generate personalized retinotopic maps directly from anatomical features. This step is crucial because anatomical variability across individuals may significantly affect electrode placement and visual outcomes. Validation in real individuals allows for more accurate predictions of functional performance.

5 CONCLUSION

In conclusion, we present an automated approach to optimize the virtual electrode placement in human visual cortex for visual neuroprostheses. It efficiently finds a suitable location yielding the closest possible match to a preset visual field coverage. We demonstrate its potential for large-scale use on a dataset comprising of anatomical and pRF data for 181 individual brains (362 hemispheres). Our open-source software (https://github.com/rickvanhoof/vimplant) can easily be expanded to facilitate different electrode configurations (including multiple arrays), different (multiple) target areas, or constraints (through different cost functions). As such, it will be able to refine surgical procedures as well as drive simulation studies in healthy observers with phosphene vision configurations that are realistic representations of the possibilities with any given electrode design.

Acknowledgements

This work was supported by the Dutch Organization for Scientific Research (NWO): STW grant number P15-42 'NESTOR', ALW grant number 823-02-010 and Cross-over grant number 17619 'INTENSE'. This work was carried out on the Dutch national e-infrastructure with the support of SURF Cooperative.

REFERENCES

Avraham, D., Jung, J., Yitzhaky, Y., & Peli, E. (2021). Retinal prosthetic vision simulation: temporal aspects. *Journal of Neural Engineering*. https://doi.org/10.1088/1741-2552/AC1B6C

Barry, M. P., Sadeghi, R., Towle, V. L., Stipp, K., Puhov, H., Diaz, W., Grant, P., Collison, F. T., Lane, F. J., Szlyk, J. P., Dagnelie, G., & Troyk, P. R. (2023). Preliminary visual function for the first human with the Intracortical Visual Prosthesis (ICVP). *Investigative Ophthalmology & Visual Science*, *64*(8), 2842. https://doi.org/10.1167/iovs.64.8.2842

Beauchamp, M. S., Oswalt, D., Sun, P., Foster, B. L., Magnotti, J. F., Niketeghad, S., Pouratian, N., Bosking, W. H., & Yoshor, D. (2020). Dynamic Stimulation of Visual Cortex Produces Form Vision in Sighted and Blind Humans. *Cell*, *181*(4), 774-783.e5. https://doi.org/10.1016/J.CELL.2020.04.033

Benson, N. C., Butt, O. H., Brainard, D. H., & Aguirre, G. K. (2014). Correction of Distortion in Flattened Representations of the Cortical Surface Allows Prediction of V1-V3 Functional Organization from Anatomy. *PLOS Computational Biology*, *10*(3), e1003538. https://doi.org/10.1371/JOURNAL.PCBI.1003538

Benson, N. C., Jamison, K. W., Arcaro, M. J., Vu, A. T., Glasser, M. F., Coalson, T. S., Essen, D. C. Van, Yacoub, E., Ugurbil, K., Winawer, J., & Kay, K. (2018). The Human Connectome Project 7 Tesla retinotopy dataset: Description and population receptive field analysis. *Journal of Vision*, *18*(13), 23–23. https://doi.org/10.1167/18.13.23

Benson, N. C., & Winawer, J. (2018). Bayesian analysis of retinotopic maps. *ELife*, *7*, 1–29.

Benson, N. C., Yoon, J. M. D., Forenzo, D., Engel, S. A., Kay, K. N., & Winawer, J. (2022). Variability of the Surface Area of the V1, V2, and V3 Maps in a Large Sample of Human Observers. *Journal of Neuroscience*, *42*(46), 8629–8646. https://doi.org/10.1523/JNEUROSCI.0690-21.2022

Beyeler, M., & Sanchez-Garcia, M. (2022). Towards a Smart Bionic Eye: AI-powered artificial vision for the treatment of incurable blindness. *Journal of Neural Engineering*, *19*(6), 063001. https://doi.org/10.1088/1741-2552/aca69d

Beyeler, M., Boynton, G. M., Fine, I., & Rokem, A. (2017). pulse2percept: A Python-based simulation framework for bionic vision. In K. Huff, D. Lippa, D. Niederhut, & M. Pacer (Eds.), Proceedings of the 16th Python in Science Conference (pp. 81-88). https://doi.org/10.25080/shinma-7f4c6e7-00c

Beyeler, M., Boynton, G. M., Fine, I., & Rokem, A. (2019). Model-Based Recommendations for Optimal Surgical Placement of Epiretinal Implants. *Med Image Comput Comput Assist Interv*, *11768*, 394-402. https://doi.org/10.1007/978-3-030-32254-0_44

Bollen, C. J. M., Guclu, U., Van Wezel, R. J. A., Van Gerven, M. A. J., & Gucluturk, Y. (2019). Simulating neuroprosthetic vision for emotion recognition. *2019 8th International Conference on Affective Computing and Intelligent Interaction Workshops and Demos, ACIIW 2019*, 85–87. https://doi.org/10.1109/ACIIW.2019.8925229

Bonizzato, M., Guay Hottin, R., Côté, S. L., Massai, E., Choinière, L., Macar, U., Laferrière, S., Sirpal, P., Quessy, S., Lajoie, G., Martinez, M., & Dancause, N. (2023). Autonomous optimization of neuroprosthetic stimulation parameters that drive the motor cortex and spinal cord outputs in rats and monkeys. *Cell Rep Med*, *4*(4), 101008. https://doi.org/10.1016/j.xcrm.2023.101008

Bosking, W. H., Oswalt, D. N., Foster, B. L., Sun, P., Beauchamp, M. S., & Yoshor, D. (2022). Percepts evoked by multi-electrode stimulation of human visual cortex. *Brain Stimulation*, *15*(5), 1163–1177. https://doi.org/10.1016/J.BRS.2022.08.007

Bradley, D. C. et al. Visuotopic Mapping Through a Multichannel Stimulating Implant in Primate V1. J Neurophysiol 93, 1659–1670 (2005).

Brindley, G. S., & Lewin, W. S. (1968). The sensations produced by electrical stimulation of the visual cortex. *The Journal of Physiology*, *196*(2), 479. https://doi.org/10.1113/JPHYSIOL.1968.SP008519

Bruce, A., Beyeler, M. (2022). Greedy Optimization of Electrode Arrangement for Epiretinal Prostheses. In: Wang, L., Dou, Q., Fletcher, P.T., Speidel, S., Li, S. (eds) Medical Image Computing and Computer Assisted Intervention – MIC-

CAI 2022. MICCAI 2022. Lecture Notes in Computer Science, vol 13437. Springer, Cham. https://doi.org/10.1007/978-3-031-16449-1_57

Chen, S., Suaning, G., Morley, J., & Lovell, N. (2009). Simulating prosthetic vision: I. Visual models of phosphenes. *Vision Research*, *49*(12), 1493–1506. https://doi.org/10.1016/J.VISRES.2009.02.003

Chen, X., Wang, F., Fernández, E., & Roelfsema, P. R. (2020). Shape perception via a high-channel-count neuroprosthesis in monkey visual cortex. *Science*, *370*(6521), 1191–1196. https://doi.org/10.1126/SCIENCE.ABD7435

Chen, X., Wang, F., Kooijmans, R., Klink, P. C., Boehler, C., Asplund, M., & Roelfsema, P. R. (2023). Chronic stability of a neuroprosthesis comprising multiple adjacent Utah arrays in monkeys. *Journal of Neural Engineering*, *20*(3), 036039. https://doi.org/10.1088/1741-2552/ACE07E

Choinière, L., Guay-Hottin, R., Picard, R., Lajoie, G., Bonizzato, M., & Dancause, N. (2024). Gaussian-process-based Bayesian optimization for neurostimulation interventions in rats. *STAR Protoc*, *5*(1), 102885. https://doi.org/10.1016/j.xpro.2024.102885

Dagnelie, G., Jiang, A., Sadeghi, R., Barry, M. P., Stipp, K., Towle, V. L., & Troyk, P. R. (2023). Constructing a phosphene map for the inaugural recipient of the intracortical visual prosthesis (ICVP). *ARVO Annual Meeting Abstract*, *June 2023*, Open Access.

Davis, T. S. et al. Spatial and temporal characteristics of V1 microstimulation during chronic implantation of a microelectrode array in a behaving macaque. J Neural Eng 9, 065003 (2012).

de Ruyter van Steveninck, J., van Gestel, T., Koenders, P., van der Ham, G., Vereecken, F., van Gerven, M., Güçlütürk, Y., & van Wezel, R. (2022). Real-world indoor mobility with simulated prosthetic vision: The benefits and feasibility of contour-based scene simplification at different phosphene resolutions. *Journal of Vision*, *22*(2), 1–1. https://doi.org/10.1167/JOV.22.2.1

de Ruyter van Steveninck, J., Nipshagen, M., van Gerven, M., Güçlü, U., Güçlütürk, Y., & van Wezel, R. (2024). Gaze-contingent processing improves mobility, scene recognition and visual search in simulated head-steered prosthetic vision. Journal of Neural Engineering, 21(2), 026037. https://doi.org/10.1088/1741-2552/ad357d

Dobelle, W. H., Mladejovsky, M. G., Evans, J. R., Roberts, T. S., & Girvin, J. P. (1976). Braille reading by a blind volunteer by visual cortex stimulation. *Nature*, *259*(5539), 111–112. https://doi.org/10.1038/259111a0

Dobelle, W. H., Mladejovsky, M. G., & Girvin, J. P. (1974). Artificial vision for the blind: Electrical stimulation of visual cortex offers hope for a functional prosthesis. *Science*, *183*(4123), 440–444. https://doi.org/10.1126/science.183.4123.440

Farnum, A., & Pelled, G. (2020). New Vision for Visual Prostheses. *Frontiers in Neuroscience*, *0*, 36. https://doi.org/10.3389/FNINS.2020.00036

Fernández, E., Alfaro, A., Soto-Sánchez, C., Gonzalez-Lopez, P., Lozano, A. M., Peña, S., Grima, M. D., Rodil, A., Gómez, B., Chen, X., Roelfsema, P. R., Rolston, J. D., Davis, T. S., & Normann, R. A. (2021). Visual percepts evoked with an intracortical 96-channel microelectrode array inserted in human occipital cortex. *The Journal of Clinical Investigation*, *131*(23). https://doi.org/10.1172/JCI151331

Fernández, E., & Normann, R. (2016). Introduction to Visual Prostheses. In: Kolb H, Fernández E, Nelson R, editors. *Webvision: The Organization of the Retina and Visual System* [Internet]. Salt Lake City (UT): University of Utah Health Sciences Center; 1995–. PMID: 27809426.

Fine, I., Boynton, G.M. A virtual patient simulation modeling the neural and perceptual effects of human visual cortical stimulation, from pulse trains to percepts. Sci Rep 14, 17400 (2024). https://doi.org/10.1038/s41598-024-65337-1

Ghezzi, D. (2023). The role of the visual field size in artificial vision. *Journal of Neural Engineering*, *20*(2), 023001. https://doi.org/10.1088/1741-2552/acc7cd

Gilissen, E., & Zilles, K. (1996). The calcarine sulcus as an estimate of the total volume of human striate cortex: a morphometric study of reliability and intersubject variability. *Journal Fur Hirnforschung*, *37*(1), 57–66. https://europepmc.org/article/med/8964978

Granley, J., & Beyeler, M. (2021). A Computational Model of Phosphene Appearance for Epiretinal Prostheses. 2021 43rd Annual International Conference of the IEEE Engineering in Medicine & Biology Society (EMBC), Mexico, 2021, pp. 4477-4481. https://doi.org/10.1109/EMBC46164.2021.9629663

Granley, J., Fauvel, T., Chalk, M., & Beyeler, M. (2023). Human-in-the-Loop Optimization for Deep Stimulus Encoding in Visual Prostheses. In A. Oh, T. Naumann, A. Globerson, K. Saenko, M. Hardt, & S. Levine (Eds.), *Advances in Neural Information Processing Systems* (Vol. 36, pp. 79376–79398).

Heitmann, C., Zhan, M., Linke, M., Hölig, C., Kekunnaya, R., van Hoof, R., Goebel, R., & Röder, B. (2023). Early visual experience refines the retinotopic organization within and across visual cortical regions. *Current Biology*, *33*(22), 4950-4959.e4. https://doi.org/10.1016/j.cub.2023.10.010

Hettick, M., Ho, E., Poole, A. J., Monge, M., Papageorgiou, D., Takahashi, K., LaMarca, M., Trietsch, D., Reed, K., Murphy, M., Rider, S., Gelman, K. R., Byun, Y. W., Hanson, T., Tolosa, V., Lee, S. H., Bhatia, S., Konrad, P. E., Mager, M., Mermel, C. H., & Rapoport, B. I. (2022). The Layer 7 Cortical Interface: A Scalable and Minimally Invasive Brain–Computer Interface Platform. *bioRxiv*, 2022.01.02.474656. https://doi.org/10.1101/2022.01.02.474656

Horton, J. C., & Hoyt, W. F. (1991). The Representation of the Visual Field in Human Striate Cortex: A Revision of the Classic Holmes Map. *Archives of Ophthalmology*, *109*(6), 816–824. https://doi.org/10.1001/ARCHOPHT.1991.01080060080030

Jung, T., Zeng, N., Fabbri, J. D., Eichler, G., Li, Z., Willeke, K., Wingel, K. E., Dubey, A., Huq, R., Sharma, M., Hu, Y., Ramakrishnan, G., Tien, K., Mantovani, P., Parihar, A., Yin, H., Oswalt, D., Misdorp, A., Uguz, I., Shinn, T., Rodriguez, G. J., Nealley, C., Gonzales, I., Roukes, M., Knecht, J., Yoshor, D., Canoll, P., Spinazzi, E., Carloni, L. P., Pesaran, B., Patel, S., Youngerman, B., Cotton, R. J., Tolias, A., & Shepard, K. L. (2024). Stable, chronic in-vivo recordings from a fully wireless subdural-contained 65,536-electrode brain-computer interface device. bioRxiv. https://doi.org/10.1101/2024.05.17.594333

Küçükoğlu, B., Rueckauer, B., Ahmad, N., van Steveninck, J. R., Güçlü, U., & van Gerven, M. (2022). Optimization of neuroprosthetic vision via end-to-end deep reinforcement learning. *International Journal of Neural Systems*, *32*(11), 2250052. https://doi.org/10.1142/S0129065722500526

Li, H., Su, X., Wang, J., Kan, H., Han, T., Zeng, Y., & Chai, X. (2018). Image processing strategies based on saliency segmentation for object recognition under simulated prosthetic vision. *Artificial Intelligence in Medicine*, *84*, 64–78. https://doi.org/10.1016/J.ARTMED.2017.11.001

Losanno, E., Badi, M., Wurth, S., Borgognon, S., Courtine, G., Capogrosso, M., Rouiller, E. M., & Micera, S. (2021). Bayesian optimization of peripheral intraneural stimulation protocols to evoke distal limb movements. *J Neural Eng*, *18*(6). https://doi.org/10.1088/1741-2552/ac3f6c

Lozano, A., Suárez, J. S., Soto-Sánchez, C., Garrigós, J., Martínez-Alvarez, J. J., Ferrández, J. M., & Fernández, E. (2020). Neurolight: A Deep Learning Neural Interface for Cortical Visual Prostheses. *International Journal of Neural Systems*, *30*(9), 2050045. https://doi.org/10.1142/S0129065720500458

Lu, Y., Wang, J., Wu, H., Li, L., Cao, X., & Chai, X. (2014). Recognition of Objects in Simulated Irregular Phosphene Maps for an Epiretinal Prosthesis. *Artificial Organs*, *38*(2), E10–E20. https://doi.org/10.1111/AOR.12174

Lycke, R., Kim, R., Zolotavin, P., Montes, J., Sun, Y., Koszeghy, A., Altun, E., Noble, B., Yin, R., He, F., Totah, N., Xie, C., & Luan, L. (2023). Low-threshold, high-resolution, chronically stable intracortical microstimulation by ultraflexible electrodes. *Cell Reports*, *42*(6), 112554. https://doi.org/10.1016/j.celrep.2023.112554

Macé, M. J.-M., Guivarch, V., Denis, G., & Jouffrais, C. (2015). Simulated Prosthetic Vision: The Benefits of Computer-Based Object Recognition and Localization. *Artificial Organs*, *39*(7), E102–E113. https://doi.org/10.1111/AOR.12476

Maureen van der Grinten, Jaap de Ruyter van Steveninck, Antonio Lozano, Laura Pijnacker, Bodo Rueckauer, Pieter Roelfsema, Marcel van Gerven, Richard van Wezel, Umut Güçlü, Yağmur Güçlütürk (2024) Towards bio-

logically plausible phosphene simulation for the differentiable optimization of visual cortical prostheses eLife 13 . https://doi.org/10.7554/eLife.85812

Maynard, E. M., Nordhausen, C. T., & Normann, R. A. (1997). The Utah Intracortical Electrode Array: A recording structure for potential brain-computer interfaces. *Electroencephalography and Clinical Neurophysiology*, *102*(3), 228-239. https://doi.org/10.1016/S0013-4694(96)95176-0

Merken, L., Schelles, M., Ceyssens, F., Kraft, M., & Janssen, P. (2022). Thin flexible arrays for long-term multi-electrode recordings in macaque primary visual cortex. *Journal of Neural Engineering*, *19*(6). https://doi.org/10.1088/1741-2552/ac98e2

Mundel, T., Milton, J. G., Dimitrov, A., Wilson, H. W., Pelizzari, C., Uftring, S., Torres, I., Erickson, R. K., Spire, J. P., & Towle, V. L. (2003). Transient inability to distinguish between faces: electrophysiologic studies. *Journal of Clinical Neurophysiology,: Official Publication of the American Electroencephalographic Society*, *20*(2), 102–110. https://doi.org/10.1097/00004691-200304000-00003

Musk, E., Neuralink. (2019). An Integrated Brain-Machine Interface Platform With Thousands of Channels. *J Med Internet Res*, *21*(10), e16194. https://doi.org/10.2196/16194

Nadolskis, L. G., Turkstra, L. M., Larnyo, E., & Beyeler, M. (2024). Great expectations: Aligning visual prosthetic development with implantee needs. *medRxiv* [Preprint]. https://doi.org/10.1101/2024.03.12.24304186

Niketeghad, S., & Pouratian, N. (2019). Brain Machine Interfaces for Vision Restoration: The Current State of Cortical Visual Prosthetics. *Neurotherapeutics*, *16*(1), 134. https://doi.org/10.1007/S13311-018-0660-1

Normann, R. A., Greger, B. A., House, P., Romero, S. F., Pelayo, F., & Fernández, E. (2009). Toward the development of a cortically based visual neuroprosthesis. *Journal of Neural Engineering*, *6*(3), 035001. https://doi.org/10.1088/1741-2560/6/3/035001

Nowik, K., Langwińska-Wośko, E., Skopiński, P., Nowik, K. E., & Szaflik, J. P. (2020). Bionic eye review – An update. *Journal of Clinical Neuroscience*, *78*, 8–19. https://doi.org/10.1016/J.JOCN.2020.05.041

Orlemann, C., Boehler, C., Kooijmans, R. N., Li, B., Asplund, M., & Roelfsema, P. R. (2024). Flexible polymer electrodes for stable prosthetic visual perception in mice. *Advanced Healthcare Materials*, *13*, 2304169. https://doi.org/10.1002/adhm.202304169

Oswalt, D., Bosking, W., Sun, P., Sheth, S. A., Niketeghad, S., Salas, M. A., Patel, U., Greenberg, R., Dorn, J., Pouratian, N., Beauchamp, M., & Yoshor, D. (2021). Multi-electrode stimulation evokes consistent spatial patterns of phosphenes and improves phosphene mapping in blind subjects. *Brain Stimulation*, *14*(5), 1356–1372. https://doi.org/10.1016/J.BRS.2021.08.024

Pedregosa, F., Michel, V., Grisel, O., Blondel, M., Prettenhofer, P., Weiss, R., Vanderplas, J., Cournapeau, D., Pedregosa, F., Varoquaux, G., Gramfort, A., Thirion, B., Grisel, O., Dubourg, V., Passos, A., Brucher, M., Perrot, M., Duchesnay, É., & Duchesnay, F. (2011). Scikit-learn: Machine Learning in Python. *Journal of Machine Learning Research*, *12*, 2825–2830. http://scikit-learn.sourceforge.net.

Perez-Yus, A., Bermudez-Cameo, J., Guerrero, J. J., & Lopez-Nicolas, G. (2017). Depth and Motion Cues with Phosphene Patterns for Prosthetic Vision. *Proceedings - 2017 IEEE International Conference on Computer Vision Workshops, ICCVW 2017*, *2018-Janua*, 1516–1525. https://doi.org/10.1109/ICCVW.2017.179

Pezaris, J. S., & Reid, R. C. (2007). Demonstration of artificial visual percepts generated through thalamic microstimulation. *PNAS*, *104*(18), 7670-7675. https://doi.org/10.1073/pnas.0608563104

Polimeni, J. R., Balasubramanian, M., & Schwartz, E. L. (2006). Multi-area visuotopic map complexes in macaque striate and extra-striate cortex. *Vision Research*, *46*(20), 3336–3359. https://doi.org/10.1016/J.VISRES.2006.03.006

Roelfsema, P. R. (2020). Writing to the Mind's Eye of the Blind. *Cell*, *181*(4), 758–759. https://doi.org/10.1016/J.CELL.2020.03.014

Rosenfeld, J., Wong, Y., Yan, E., & Lowery, A. (2020). Tissue response to a chronically implantable wireless intracortical visual prosthesis (Gennaris array). *Iopscience.Iop.Org*. https://iopscience.iop.org/article/10.1088/1741-2552/ab9e1c/meta

Rosenke, M., van Hoof, R., van den Hurk, J., Grill-Spector, K., & Goebel, R. (2021). A Probabilistic Functional Atlas of Human Occipito-Temporal Visual Cortex. *Cerebral Cortex*, *31*(1), 603–619. https://doi.org/10.1093/CERCOR/BHAA246

Sahasrabuddhe, K., Khan, A. A., Singh, A. P., Stern, T. M., Ng, Y., Tadić, A., Orel, P., LaReau, C., Pouzzner, D., Nishimura, K., Boergens, K. M., Shivakumar, S., Hopper, M. S., Kerr, B., Hanna, M.-E. S., Edgington, R. J., McNamara, I., Fell, D., Gao, P., Babaie-Fishani, A., Veijalainen, S., Klekachev, A. V., Stuckey, A. M., Luyssaert, B., Kozai, T. D. Y., Xie, C., Gilja, V., Dierickx, B., Kong, Y., Straka, M., Sohal, H. S., & Angle, M. R. (2020). The Argo: A 65,536 channel recording system for high density neural recording in vivo. *bioRxiv*, 2020.07.17.209403. https://doi.org/10.1101/2020.07.17.209403

Salzman, C. D., Britten, K. H., & Newsome, W. T. (1990). Cortical microstimulation influences perceptual judgements of motion direction. *Nature 1990 346:6280*, *346*(6280), 174–177. https://doi.org/10.1038/346174a0

Sanchez-Garcia, M., Martinez-Cantin, R., & Guerrero, J. J. (2018). *Structural and object detection for phosphene images*. http://arxiv.org/abs/1809.09607

Sanchez-Garcia, M., Martinez-Cantin, R., & Guerrero, J. J. (2020). Semantic and structural image segmentation for prosthetic vision. *PLOS ONE*, *15*(1), e0227677. https://doi.org/10.1371/JOURNAL.PONE.0227677

Schalk, G., Brunner, P., Allison, B.Z., et al. (2024). Translation of neurotechnologies. *Nature Reviews Bioengineering*. https://doi.org/10.1038/s44222-024-00185-2

Schiller, P. H., Slocum, W. M., Kwak, M. C., Kendall, G. L., & Tehovnik, E. J. (2011). New methods devised specify the size and color of the spots monkeys see when striate cortex (area V1) is electrically stimulated. *Proceedings of the National Academy of Sciences of the United States of America*, *108*(43), 17809–17814. https://doi.org/10.1073/PNAS.1108337108/SUPPL_FILE/PNAS.201108337SI.PDF

Schmidt, E. M., Bak, M. J., Hambrecht, F. T., Kufta, C. V., O'Rourke, D. K., & Vallabhanath, P. (1996). Feasibility of a visual prosthesis for the blind based on intracortical micro stimulation of the visual cortex. *Brain*, *119*(2), 507–522. https://doi.org/10.1093/BRAIN/119.2.507

Schwartz, E. L. (1983). Cortical mapping and perceptual invariance: A reply to cavanagh. *Vision Research*, *23*(8), 831–835. https://doi.org/10.1016/0042-6989(83)90206-7

Seabold, S., & Perktold, J. (2010). *statsmodels: Econometric and statistical modeling with python*. In 9th Python in Science Conference.

Sehgal, S. N., & Farooq, S. A. (2021). 3D Time-of-Flight MRA. In Neuroimaging Techniques (pp. 77-80). Springer. https://doi.org/10.1007/978-3-030-85413-3_77

Shahriari, B., Swersky, K., Wang, Z., Adams, R. P., & De Freitas, N. (2016). Taking the human out of the loop: A review of Bayesian optimization. *Proceedings of the IEEE*, *104*(1), 148–175. https://doi.org/10.1109/JPROC.2015.2494218

Steveninck, J. de R. van, Güçlü, U., Wezel, R. van, & Gerven, M. van. (2020). End-to-end optimization of prosthetic vision. *BioRxiv*, 2020.12.19.423601. https://doi.org/10.1101/2020.12.19.423601

Tehovnik, E. J., Slocum, W. M., Carvey, C. E., & Schiller, P. H. (2005). Phosphene Induction and the Generation of Saccadic Eye Movements by Striate Cortex. *Https://Doi.Org/10.1152/Jn.00736.2004*, *93*(1), 1–19. https://doi.org/10.1152/JN.00736.2004

Tehovnik, E. J., Tolias, A. S., Sultan, F., Slocum, W. M., & Logothetis, N. K. (2006). Direct and indirect activation of cortical neurons by electrical microstimulation. *Journal of Neurophysiology*, *96*(2), 512–521. https://doi.org/10.1152/JN.00126.2006/ASSET/IMAGES/LARGE/Z9K0080675760003.JPEG

Van Der Grinten, M., De Ruyter Van Steveninck, J., Lozano, A., Pijnacker, L., Rückauer, B., Roelfsema, P., Van Gerven, M., Van Wezel, R., Güçlü, U., & Gmur Güçlütürk, Y. ̆. (2022). Biologically plausible phosphene simulation for the differentiable optimization of visual cortical prostheses. *BioRxiv*, 2022.12.23.521749. https://doi.org/10.1101/2022.12.23.521749

Vergnieux, V., Macé, M. J.-M., & Jouffrais, C. (2017). Simplification of Visual Rendering in Simulated Prosthetic Vision Facilitates Navigation. *Artificial Organs*, *41*(9), 852–861. https://doi.org/10.1111/AOR.12868

Virtanen, P., Gommers, R., & Oliphant, T. E. (2020). SciPy 1.0: fundamental algorithms for scientific computing in Python. *Nature Methods*, *17*(3), 261–272. https://doi.org/10.1038/S41592-019-0686-2

Viviani, R. (2016). A digital atlas of middle to large brain vessels and their relation to cortical and subcortical structures. Frontiers in Neuroanatomy, 10, 12. https://doi.org/10.3389/fnana.2016.00012

Wandell, B., Dumoulin, S., & Brewer, A. (2007). Visual Field Maps in Human Cortex. *Neuron*, *56*(2), 366–383. https://doi.org/10.1016/J.NEURON.2007.10.012

Wang, J., Zhu, H., Liu, J., Li, H., Han, Y., Zhou, R., & Zhang, Y. (2021). The application of computer vision to visual prosthesis. *Artificial Organs*. https://doi.org/10.1111/AOR.14022

Wang, L., Mruczek, R. E. B., Arcaro, M. J., & Kastner, S. (2015). Probabilistic Maps of Visual Topography in Human Cortex. *Cerebral Cortex*, *25*(10), 3911–3931. https://doi.org/10.1093/CERCOR/BHU277

Wang, L., Yang, L., & Dagnelie, G. (2008). Virtual Wayfinding Using Simulated Prosthetic Vision in Gaze-locked Viewing. *Optometry and Vision Science,: Official Publication of the American Academy of Optometry*, *85*(11), E1057. https://doi.org/10.1097/OPX.0B013E31818B9F36

Winawer, J. & Parvizi, J. Linking Electrical Stimulation of Human Primary Visual Cortex, Size of Affected Cortical Area, Neuronal Responses, and Subjective Experience. Neuron 92, 1213–1219 (2016).

Xia, P., Hu, J., & Peng, Y. (2015). Adaptation to Phosphene Parameters Based on Multi-Object Recognition Using Simulated Prosthetic Vision. *Artificial Organs*, *39*(12), 1038–1045. https://doi.org/10.1111/AOR.12504

Yang, G., Zhou, S., Bozek, J., Dong, H. M., Han, M., Zuo, X. N., Liu, H., & Gao, J. H. (2020). Sample sizes and population differences in brain template construction. *NeuroImage*, *206*, 116318. https://doi.org/10.1016/J.NEUROIMAGE.2019.116318

Zhao, Y., Li, X., & Wang, Z. (2024). Flexible, scalable, high channel count stereo-electrode for large-scale recording of human single neuron activity. *Nature Communications*, *14*, Article 43727. https://doi.org/10.1038/s41467-023-43727-9